Robert Pietzsch
e-mail: r.pietzsch@fh-sm.de

Miroslaw Brzoza
e-mail: miroslaw.brzoza@vst.uni-magdeburg.de

Yalçin Kaymak
e-mail: yalcin.kaymak@student.uni-magdeburg.de

Eckehard Specht
e-mail: eckehard.specht@vst.uni-magdeburg.de

Institut für Strömungstechnik und
Thermodynamik,
Universitätsplatz 2,
39106 Magdeburg, Germany

Albrecht Bertram
Institut für Mechanik,
Universitätsplatz 2,
39106 Magdeburg, Germany
e-mail: Bertram@mb.uni-magdeburg.de

Simulation of the Distortion of Long Steel Profiles During Cooling

A complex thermomechanical model for simulating the transient fields of the temperature, microstructure, stress, strain, and displacement during quenching of steel profiles is introduced. The thermoplastic material model is formulated on the basis of J_2-plasticity theory with a temperature- and phase fraction-dependent yield limit. Coupling effects such as dissipation, phase transformation enthalpy, and transformation-induced plasticity are considered. The validity of the model is verified by comparing the simulation results with available experimental measurements. The introduced model serves as a basis for optimizing the cooling conditions for reducing residual stresses and distortions. The simulation results for T and L profiles of two different types of steel are described.
[DOI: 10.1115/1.2338050]

1 Introduction

Quenching processes are applied to long steel profiles after the rolling process to produce profiles with reliable service properties. The typical problem is the distortion that is occurring upon residual stresses. Profile distortion should be eliminated as it leads to rework expenditure and creates problems associated with bearing and bundling. Moreover, the residual stresses should be controlled to prevent the crack initiation. The modeling of the cooling process is difficult due to the complicated couplings among different physical and mechanical processes [1]. The main reason for the distortion is the inhomogeneity of the temperature profile during the cooling process which results in residual stresses, varying phase fractions, etc. [2]. The cooling distortion of railway profiles has already been extensively investigated by experiments. An overview of the works can be found in the literature [3], where the experimental results for the residual stresses and deformations after quenching are presented. The distortion and residual stresses in carburized thin strips are investigated by Prantil et al. [4].

The thermoplasticity and metallurgical transformations establish the fundamental part of the problem. The distortion is due to transformation-induced stresses and thermal stresses. The phase transitions, temperature, and stresses must be accurately simulated to determine the distortion. If the temperature and cooling conditions are constant in the axial direction of the profile, all the other fields are also constant. Consequently, a 2D mathematical model with fewer degrees of freedom is enough for the simulations. This reduction of the dimension simplifies not only the visualization of the fields, but also the determination of the optimal cooling conditions. This work indicates that the distortion can be significantly reduced by an intensified cooling of the mass lumped parts of the cross section. The atomized spray quenching technique [5,6], where the spraying water is atomized into fine droplets by means of compressed air, is suitable to intensify the cooling of the mass lumped regions, since the vapor film, which occurs in other quenching techniques, is avoided. In this way the mass lumped regions of the workpieces can be cooled more intensively than the edges. Consequently, a uniform temperature distribution on the surface and a reduced stress distribution inside the body with reduced distortion can be obtained.

2 Mathematical Modeling

In the following sections, the details of the mathematical model for the temperature, microstructure, and stress computations are given. Moreover, the distortion measure and the solution algorithm used for computation are briefly described.

2.1 Temperature Field. The temperature field is modeled by Fourier's law of heat conduction with two additional heat source terms. The first additional term accounts for the transformation enthalpies, and the second term includes the heat generation by mechanical energy dissipation. During the quenching processes, the heat generated due to the mechanical work is negligibly small as compared to the transformation enthalpies. The Fourier's law is

$$\frac{\partial}{\partial x}\left(k\frac{\partial T}{\partial x}\right)+\frac{\partial}{\partial y}\left(k\frac{\partial T}{\partial y}\right)+\frac{\partial}{\partial z}\left(k\frac{\partial T}{\partial z}\right)+q_v=\rho c_p\frac{\partial T}{\partial t} \tag{1}$$

with boundary condition

$$k\frac{\partial T}{\partial \mathbf{n}_S}+q_S=0. \tag{2}$$

In Eqs. (1) and (2) k is the heat conductivity, q_v is the heat source, ρ is the mass density, c_p is the specific heat, q_S is the heat flux through the body surface, and $\mathbf{n}_S$ is the surface unit normal. All of the material constants are assumed to be functions of the temperature T and the converted phase fractions ξ_i. The dependency of the material properties on the phase fractions ξ_i can be expressed by the arithmetic, geometric, harmonic, or other means.

Contributed by the Applied Mechanics Division of ASME for publication in the JOURNAL OF APPLIED MECHANICS. Manuscript received September 28, 2005; final manuscript received May 21, 2006. Review conducted by Z. Suo. Discussion on the paper should be addressed to the Editor, Prof. Robert M. McMeeking, Journal of Applied Mechanics, Department of Mechanical and Environmental Engineering, University of California–Santa Barbara, Santa Barbara, CA 93106-5070, and will be accepted until four months after final publication of the paper itself in the ASME JOURNAL OF APPLIED MECHANICS.

The heat flux q_S through the boundary and internal heat source q_v are

$$q_S = \psi \cdot e \cdot \sigma(T^4 - T_\infty^4) + \alpha(T - T_\infty) = \alpha'(T - T_\infty)$$

$$q_v = \chi \sigma_y \dot{\varepsilon}_{\text{eff}}^p + \Sigma_{i=1}^n L_i \cdot \dot{\xi}_i \tag{3}$$

The heat flux q_S is due to thermal radiation and heat convection, where α' is the equivalent convection coefficient, T is the temperature of the body surface, T_∞ is the ambient temperature, ψ is the view factor, e is the emissivity, and σ is the Stefan Boltzmann constant. The internal heat source q_v is composed of latent heat generation and dissipation of mechanical energy into heat, where L_i are the latent heats of transformation, $\dot{\xi}_i$ are the rates of phase conversion, χ is the fraction of mechanical energy converted to heat energy, σ_y is the yield strength, and $\dot{\varepsilon}_{\text{eff}}^p$ is the rate of effective plastic strain.

The finite element method is used to solve Eq. (1). For the case of simplified (plane stress, plane strain, axis symmetric, and beam case) 2D simulations, the six-node isoparametric triangular element is implemented. The temperature field in the element is approximated by

$$T^e \cong \Sigma_{i=1}^N H_i^e T_i^e, \tag{4}$$

where T_i^e are the element nodal temperatures, and N is the number of nodes in the element. The quadratic element interpolation functions are

$$\mathbf{H}^e = \begin{bmatrix} 1 - 3(r+s) + 2(r+s)^2 \\ 4r(1-r-s) \\ r(2r-1) \\ 4 \\ s(2s-1) \\ 4s(1-r-s) \end{bmatrix}. \tag{5}$$

The domain is subdivided into finite elements and the temperature of each element is represented by using element nodal temperatures T_i^e and interpolation functions H_i^e. With this substitution, the differential equation and the boundary condition are not identically satisfied, but are instead equal to an error term. The interpolation functions are used as weight functions and the Galerkin's method is applied to minimize this error term and to get the system of linear algebraic equations

$\mathbf{KT} + \mathbf{C}\dot{\mathbf{T}} = \mathbf{F}$ where

$$K_{ij} = \Sigma_{e=1}^{Nel} \int_{A^e} \nabla H_i^e k \nabla H_j^e h dA + \Sigma_{e=1}^{Nel} \int_{S^e} H_i^e \alpha' H_j^e h dS,$$

$$C_{ij} = \Sigma_{e=1}^{Nel} \int_{A^e} H_i^e \rho c_p H_j^e h dA,$$

$$F_i = \Sigma_{e=1}^{Nel} \int_{A^e} H_i^e q_v h dA + \Sigma_{e=1}^{Nel} \int_{S^e} H_i^e \alpha' T_\infty h dS \tag{6}$$

The surface integrals are calculated only for those elements that lay on the boundary. The summation symbol stands for an assembly operator to construct the finite element system matrices.

The material properties of the phase mixture are calculated by using the phase fractions and material properties of constituting phases. Different homogenization methods are applied for different material properties. The generalized homogenization equation is given by

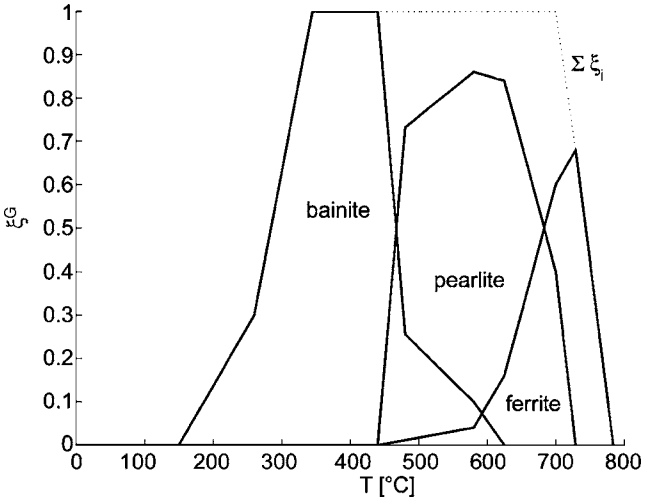

Fig. 1 Equilibrium microstructure fraction for C45 steel

$$Z_{\text{mix}} = \left(\Sigma_{i=1}^n \xi_i Z_i^N\right)^{\frac{1}{N}}, \tag{7}$$

where Z_{mix} stands for the mixture material property estimate and Z_i for the material property of ith phase. The arithmetic mean is assumed for the density ρ, heat conductivity k, or heat capacity c_p with a value of $N=1$. The harmonic mean is assumed for the flow stress σ_y with a value of $N=-1$. The geometric mean, $Z_{\text{mix}} = \exp[\Sigma_{i=1}^n \xi_i \ln(Z_i)]$, is assumed for the bulk modulus κ or the shear modulus μ with a value of $N=0$.

2.2 Microstructure Field. The mathematical theory of the phase transformation kinetics is still not well established. In general, the time-temperature-transformation (TTT) diagrams which are derived from experiments are used. Isothermal transformation (IT) diagrams are convenient, since continuous cooling transformation (CT) diagrams for an arbitrary cooling process can be calculated from IT diagrams by the methods described in literature [7–11].

There are two different types of phase transformation, namely diffusional and martensitic transformations. For diffusional transformations, the formation of the new phase is described by the Kolmogorov-Johnson-Mehl-Avrami [12] equation,

$$\xi_i = \xi_i^{eq}[1 - \exp\{-a_i \cdot (t^{\text{iso}})^{b_i}\}], \tag{8}$$

under isothermal conditions with temperature-dependent transformation parameters a_i and b_i for each phase. After an infinitely long time, the phases achieve their equilibrium fractions ξ_i^{eq}. These equilibrium fractions are shown in Fig. 1 for the steel C45.

The transformation limit curves in the IT diagrams contain two C-shaped curves for each phase transition. One is for the beginning of the transformation and the other is for its end. Each curve is approximated by the equation

$$\tau(T) = d_0 \cdot \exp \frac{d_1 + d_2 (T_U - T)^{-n}}{T - T_L}, \tag{9}$$

which is proposed by Hougardy [13]. Here, T_L and T_U are the lower and upper asymptotes of the curve, respectively. The other parameters d_0, d_1, and d_2 are uniquely defined if three points $\{(t_1, T_1), (t_2, T_2), (t_3, T_3)\}$ on the limit curve and the exponent n are given

$$d_0 = t_1 \exp\left[\frac{(T_3 - T_L)(\varphi_{13} - \varphi_{23})\ln\left(\frac{t_1}{t_3}\right) + (T_L - T_2)(\varphi_{12} - \varphi_{23})\ln\left(\frac{t_1}{t_2}\right)}{(T_1 - T_2)\varphi_{12} + (T_3 - T_1)\varphi_{13} + (T_2 - T_3)\varphi_{23}}\right],$$

$$d_1 = \frac{\varphi_{23}[T_2T_3 - T_L(T_2 + T_3) + T_L^2] - \varphi_{12}[T_1T_2 - T_L(T_1 + T_2) + T_L^2]}{(T_1 - T_2)\varphi_{12} + (T_3 - T_1)\varphi_{13} + (T_2 - T_3)\varphi_{23}}\ln\left(\frac{t_1}{t_2}\right)$$
$$+ \frac{\varphi_{13}[T_1T_3 - T_L(T_1 + T_3) + T_L^2] - \varphi_{23}[T_2T_3 - T_L(T_2 + T_3) + T_L^2]}{(T_1 - T_2)\varphi_{12} + (T_3 - T_1)\varphi_{13} + (T_2 - T_3)\varphi_{23}}\ln\left(\frac{t_1}{t_2}\right),$$

$$d_2 = \frac{(T_3 - T_L)(T_2 - T_1)\ln\left(\frac{t_1}{t_2}\right) + (T_3 - T_1)(T_L - T_2)\ln\left(\frac{t_1}{t_2}\right)}{(T_1 - T_2)\varphi_{12} + (T_3 - T_1)\varphi_{13} + (T_2 - T_3)\varphi_{23}}\varphi_{123}, \tag{10}$$

where

$$\varphi_{12} = \{(T_1 - T_U)(T_2 - T_U)\}^n,$$

$$\varphi_{13} = \{(T_1 - T_U)(T_3 - T_U)\}^n,$$

$$\varphi_{23} = \{(T_2 - T_U)(T_3 - T_U)\}^n,$$

$$\varphi_{123} = \{-(T_1 - T_U)(T_2 - T_U)(T_3 - T_U)\}^n. \tag{11}$$

The transformation beginning curve gives the beginning time t_B^{iso} when 1% of the new phase fraction is formed. The other curve gives the transformation end time t_E^{iso} when 99% of the equilibrium phase fraction ξ^{eq} is formed at a constant temperature T

$$1 - \exp\{-a \cdot (t_B^{\text{iso}})^b\} = 0.01$$

$$1 - \exp\{-a \cdot (t_E^{\text{iso}})^b\} = 0.99\xi^{eq}. \tag{12}$$

The transformation parameters a and b are obtained by solving Eq. (12)

$$a = -\frac{1}{(t_E^{\text{iso}})^b}\ln(1 - 0.99\xi^{eq})$$

$$b = \frac{1}{\ln\left(\frac{t_S^{\text{iso}}}{t_E^{\text{iso}}}\right)}\ln\left[\frac{\ln(1 - 0.01)}{\ln(1 - 0.99\xi^{eq})}\right], \tag{13}$$

at a constant temperature T, if the beginning time t_B^{iso} and the end time t_E^{iso} are known. The variations of these factors with respect to the temperature are shown in Fig. 2 for C45.

In the continuous cooling case, the transformation begins at the incubation time t_B^{inc} and it ends after time t_E^{inc}, which are obtained by Scheil's sum [14]

$$\int_0^{t_{S,E}^{\text{inc}}} \frac{1}{\tau_{B,E}[T(t)]}dt = 1, \tag{14}$$

on discrete basis

$$\Sigma_{i=1}^{n}\frac{\Delta t}{\tau_{B,E}(T_i)} = 1, \tag{15}$$

for an arbitrary cooling curve $T(t)$.

The calculations are much easier for martensitic transformations that do not depend directly on the time but only on the temperature. The martensite phase fraction is calculated according to Koistinen-Marburger [15] equation

$$\xi_M = \xi_A\{1 - \exp[-k_M(T_{Ms} - T)]\}, \tag{16}$$

where ξ_A is the austenite phase fraction at the beginning of martensitic transformation, k_M is a stress-dependent transformation constant, and T_{Ms} is the temperature at which the martensitic transformation starts. The effects of the stress state on the transformation kinetics are discussed by Denis et al. [16].

2.3 Stress/Strain Field. An isotropic thermoplastic material behavior with a temperature and phase fraction dependent constitutive relation is employed. The basic assumptions are as follows:

A1: total deformations are small,

$$\mathbf{E} = 1/2(\text{grad}(\mathbf{u}) + \text{grad}^T(\mathbf{u})) \text{ and } \mathbf{E} = \mathbf{E}^{T,\xi} + \mathbf{E}^p + \mathbf{E}^{\text{trip}} + \mathbf{E}^e; \tag{17}$$

A2: the material is isotropic,

$$\mathbf{T} = \mathbf{C}[\mathbf{E}^e] = \kappa\,\text{tr}(\mathbf{E} - \mathbf{E}^{T,\xi})\mathbf{I} + 2\mu(\mathbf{E}' - \mathbf{E}^{\text{trip}} - \mathbf{E}^p); \tag{18}$$

A3: plastic deformations are incompressible,

$$\text{tr}(\mathbf{E}^p) = 0, \quad \mathbf{E}'^p = \mathbf{E}^p; \tag{19}$$

A4: the material behavior is rate independent,
A5: the flow condition is of von Mises type,

$$\phi(\mathbf{T}', \varepsilon^p, T, \xi_i) = \|\mathbf{T}'\| - \sqrt{2/3}\sigma_y(\varepsilon^p, T, \xi_i) \tag{20}$$

A6: an associative plastic model is used,

$$\dot{\mathbf{E}}^p = \lambda\frac{\partial\varphi}{\partial T} = \lambda\frac{\mathbf{T}'}{\|\mathbf{T}'\|} = \lambda\mathbf{N}'; \text{and} \tag{21}$$

A7: linear isotropic hardening behavior is assumed,

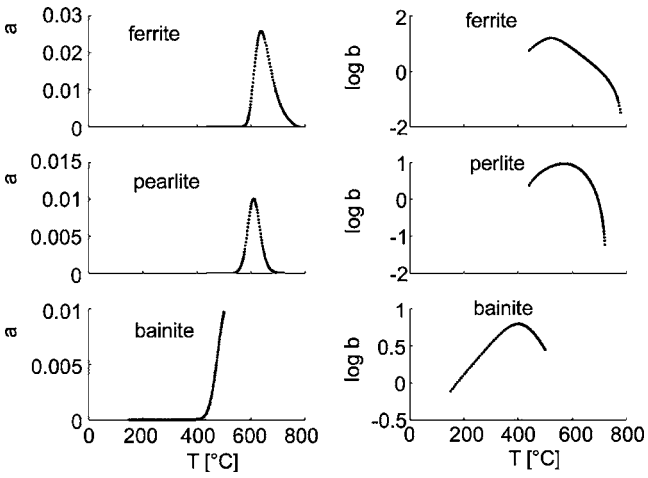

Fig. 2 Avrami constant of transformation kinetics

$$\sigma_y = \sigma_{yvmix}^{HM} + H_{mix}^{HM}\varepsilon^p, \dot{\varepsilon}^p = \sqrt{2/3}\lambda. \tag{22}$$

The prime "$\mathbf{N}'$" over a tensor represents its deviator, "tr($\mathbf{E}$)" is the trace operator.

Material equations

$$\text{loading condition: } \dot{\phi}|_{\varepsilon^p=\text{const.}} \frac{\partial \phi}{\partial \mathbf{T}'} \cdot \dot{\mathbf{T}}' + \frac{\partial \phi}{\partial T}\dot{T} + \Sigma_{i=1}^{n} \frac{\partial \phi}{\partial \xi_i}\dot{\xi}_i = \begin{cases} >0 \text{ loading} \\ =0 \text{ neutral} \\ <0 \text{ unloading} \end{cases} \tag{23}$$

$$\text{consistency condition: } \dot{\phi} = \frac{\partial \phi}{\partial \mathbf{T}'} \cdot \dot{\mathbf{T}}' + \frac{\partial \phi}{\partial \varepsilon^p}\dot{\varepsilon}^p + \frac{\partial \phi}{\partial T}\dot{T} + \Sigma_{i=1}^{n} \frac{\partial \phi}{\partial \xi_i}\dot{\xi}_i = 0. \tag{24}$$

For a plastic loading increment, the unknown plastic multiplier λ can be obtained from the consistency condition Eq. (24). The first term in the consistency condition is computed from the elastic law Eq. (18)

$$\frac{\partial \varphi}{\partial \mathbf{T}'} \cdot \dot{\mathbf{T}}' = \mathbf{N}' \cdot \{2\dot{\mu}(\mathbf{E} - \mathbf{E}^{\text{trip}} - \mathbf{E}^p) + 2\mu(\dot{\mathbf{E}} - \dot{\mathbf{E}}^{trip} - \dot{\mathbf{E}}^p)\}. \tag{25}$$

Equations (20)–(22) are used to calculate the last three terms in the consistency condition. Finally, the unknown plastic multiplier is

$$\lambda = \frac{2\dot{\mu}\mathbf{N}' \cdot (\mathbf{E} - \mathbf{E}^{\text{trip}}) + 2\mu\mathbf{N}' \cdot (\dot{\mathbf{E}} - \dot{\mathbf{E}}^{\text{trip}}) - \sqrt{\frac{2}{3}}\left(\frac{\partial \sigma_y}{\partial T}\dot{T} + \Sigma_{i=1}^{n}\frac{\partial \sigma_y}{\partial \xi_i}\dot{\xi}_i\right)}{2\mu + \frac{2}{3}H}. \tag{26}$$

A linear relation between temperature and thermal strain is used in general. However, this method contains a linearization [17] and sometimes requires a conversion of the reference temperatures. An alternative method is based on the temperature dependence of the density [18]. The thermal and transformation induced strains are combined in an isotropic tensor

$$\mathbf{E}^{T,\xi} = \left(\sqrt[3]{\frac{\rho_R}{\rho}} - 1\right)\mathbf{I}, \tag{27}$$

where ρ_R denotes the reference density and ρ is the mixture density. For an n-phase mixture, the thermal and transformation induced strain rate becomes

$$\dot{\mathbf{E}}^{T,\xi} = \frac{d\mathbf{E}^{T,\xi}}{d\rho}\left(\frac{\partial \rho}{\partial T}\dot{T} + \Sigma_{i=1}^{n}\frac{\partial \rho}{\partial \xi_i}\dot{\xi}_i\right). \tag{28}$$

The transformation induced plasticity (TRIP) is an additional irreversible deformation, which occurs during the phase transition. The TRIP flow occurs in the direction of the stress deviator $\mathbf{T}'$, even if the global stress does not exceed the yield limit of a single phase. The flow rate is proportional to the phase transition rate and the stress deviator

$$\dot{\mathbf{E}}^{\text{trip}} = -\frac{3}{2}\Lambda \ln(\xi)\dot{\xi}\mathbf{T}'. \tag{29}$$

This equation characterizes the macroscopic material behavior, which is determined by the micromechanical processes. Moreover, the proportionality factor depends on the fraction of the transformed phase and Greenwood Johnson coefficient Λ [19], which must be determined experimentally. The equation for the factor is given as

$$\Lambda_i = \frac{5(\rho_A - \rho_i)}{6\rho_A\sigma_{yA}}, \tag{30}$$

where the density ratio is a measure for the volume ratio of the converting phases (e.g. austenite, pearlite) and σ_{yA} the yield limit of the softer phase (mostly austenite) at transformation temperature.

The relationship between the stress tensor $\mathbf{T}$ and the elastic strain tensor $\mathbf{E}^e$ is given by the elastic law Eq. (18). The tangential elastoplastic material operator is

$$\mathbf{C}^{ep} = \left.\frac{\partial \mathbf{T}}{\partial \mathbf{E}^{ep}}\right|_{T,\xi=\text{const.}} = \mathbf{C}^e - \frac{2\mu}{1 + \frac{H}{3\mu}}\mathbf{N}' \otimes \mathbf{N}' = 3\kappa\mathbf{I} \otimes \mathbf{I} + 2\mu\left(\mathbf{I} - \tfrac{1}{3}\mathbf{I} \otimes \mathbf{I}\right) - \frac{2\mu}{1 + \frac{H}{3\mu}}\mathbf{N}' \otimes \mathbf{N}', \tag{31}$$

where $\mathbf{I}$ is fourth order identity tensor and $\mathbf{I} \otimes \mathbf{I}$ the dyadic product of second order identity tensors. Quadratic convergence is provided for plastic deformations with the elastoplastic tangential operator.

2.4 Description of the Distortion. The distortion of long steel profiles is intended to be simulated by the model described above. The distortion cannot be adequately described by the deflection of the profile as it depends on the length of the profile. Hence, the distortion is defined in terms of curvature of profile. The deflection Δ from the neutral axis is approximated by a parabola

$$\Delta = p \cdot z^2. \tag{32}$$

The curvature related factor p serves as a measure for the distortion.

2.5 Solution Algorithm. A time integration scheme that involves equilibrium iterations at each time step is applied to solve the coupled field problem described above. In an iteration step, first the temperature, phase transitions and stress field are calculated, respectively. The phase transitions are calculated by using the current iteration temperature and the temperature from the previous time step. When the values of temperature, microstructure fractions and stresses have converged, the iteration for the next time step is started.

3 Experimental Verification of Mathematical Model

The simulation results were compared with the experimental measurements in order to validate the mathematical model introduced above. As no proper measurements for profiles are known, we used the available experimental results for notched shafts and

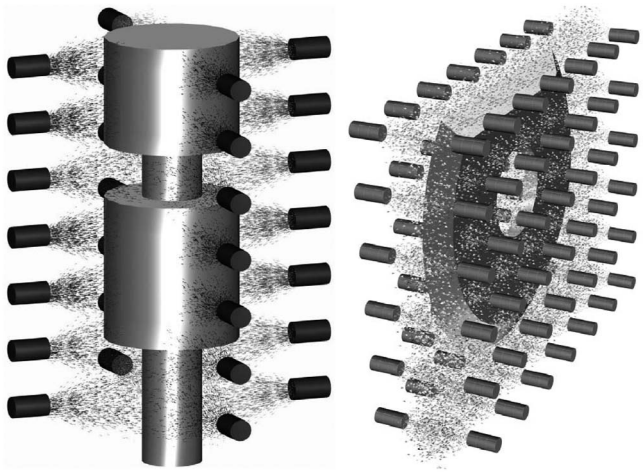

Fig. 3 The shaft (α=450 W/m^2/K) and the disk (α =200 W/m^2/K) with the quenching nozzle field

cutting disks as shown in Fig. 3. The samples were homogeneously heated in a roller-hearth kiln up to a temperature value of 850°C in a nitrogen atmosphere. After the heating, the samples fell into a catching cage, in which they were precisely positioned and quenched in a nozzle field. The nozzle spacing, flow rate, and distance from the sample could be adjusted. The heat transfer coefficient could be controlled in this way and was well known from other specific measurements. Samples were available in two geometries, i.e., shafts; 18 mm in diameter with 60 mm of length, and 36 mm in diameter with 120 mm of length, and disks; 90 mm and 120 mm of outer diameter. As a material, 100Cr6 was used because the material properties are well known and available with high accuracy as given in Table 1. Further details of the experiments can be found in the literature [20].

The temperatures were measured with thermocouples of type K and class 1, which have an accuracy of 1.5°C for 0–375°C and 0.004T °C for 375–1000°C. The thermocouples were placed in the drilled holes as shown in Fig. 4. The regions 2 and 3 have the highest and lowest temperatures, respectively. As an example, the measured temperatures at these two points are compared to the calculated ones for the bigger shaft. As expected, the curves coincide for an appropriate heat transfer coefficient.

The calculated stresses are compared to the measured stresses for the bigger shaft in Fig. 5. The measurements are performed at five sampling points in longitudinal direction with a computer-controlled diffractometer. The simulation result matches well the measurements as it can be seen in Fig. 5.

Table 2 presents the calculated and measured microstructure fractions for the shafts and disks. The probes were taken from the positions at the surface given in the upper-left corner of Table 2. The microstructure fractions were measured by the point analysis method [21] with an accuracy of 1% fraction. The calculated martensite fraction values were higher for the shafts but smaller for the disks than those measured. The calculated bainite fraction was slightly lower than the measured values for the small shaft, and for all other cases it was slightly higher. Calculated and measured pearlite fractions occurred only for the shafts and these values are similar. The discrepancies with the experimental measurements are less than 10% mostly and they are acceptable for such simulations. Such a behavior might be due to small fluctuations of chemical compositions which are listed in Table 3.

The distortion of the cutting disk was measured by the change in the radius of a hole with accuracy 1.3 μm. Figure 6 shows the radial displacement of the hole in the angular position. As can be seen from Fig. 6, the simulation results fit the measured distortion of the disks.

The overall performance of the model is quite satisfactory, and the finite element simulation results are in agreement with the measurements. The mesh convergence tests have been performed and it is observed that further refinements of the mesh have neg-

Table 1 Material properties for 100Cr6

Pearlite & Martensite							
Temperature (°C)	Elasticity Modulus (GPa)	Poisson's Ratio	Yield Strength (MPa)	Hardening Modulus (GPa)	Density (kg/m^3)	Heat Conductivity (W/m/K)	Heat Capacity (J/kg/K)
0	212	0.283	479- 1116	21- 63	7820	40.0	410
200	202	0.291	472- 914	26- 40	7740	39.0	550
400	186	0.299	400- 712	22- 17	7770	35.5	620
600	166	0.307	277- 510	19- 0	7620	29.0	790
800	141	0.315	118- 0	11- 0	7530	20.0	1160
1000	112	0.323	0- 0	0- 0	7460	8.5	1850
Austenite							
Temperature (°C)	Elasticity Modulus (GPa)	Poisson's Ratio	Yield Strength (MPa)	Hardening Modulus (GPa)	Density (kg/m^3)	Heat Conductivity (W/m/K)	Heat Capacity (J/kg/K)
0	212	0.283	300	12.0	7980	14.5	450
200	202	0.291	270	10.4	7900	17.2	510
400	186	0.299	240	8.8	7820	19.9	570
600	166	0.307	210	7.2	7720	22.6	600
800	141	0.315	180	5.6	7620	25.3	630
1000	112	0.323	150	4.0	7530	28.0	650

Pearlite & Martensite							
Temperature (°C)	Elasticity Modulus (GPa)	Poisson's Ratio	Yield Strength (MPa)	Hardening Modulus (GPa)	Density (kg/m^3)	Heat Cunductivity (W/m/K)	Heat Capacity (J/kg/K)
0	215	83	550-1000	5.1-12.5	7850	48.8	410
200	196	75	420-940	5.8-10.0	7790	46.5	550
400	177	67	470-800	4.9-7.5	7710	41.0	620
600	158	59	470-0	2.6-0	7630	35.0	790
800	140	52	180-0	0-0	7530	26.0	1160
1000	121	44	0-0	0-0	7430	17.0	1850
Austenite							
Temperature (°C)	Elasticity Modulus (GPa)	Poisson's Ratio	Yield Strength (MPa)	Hardening Modulus (GPa)	Density (kg/m^3)	Heat Cunductivity (W/m/K)	Heat Capacity (J/kg/K)
0	200	80	250	4.2	7940	14.8	450
200	160	64	200	4.0	7860	17.3	510
400	120	48	150	3.7	7790	19.6	570
600	80	32	100	3.1	7700	21.9	600
800	40	16	50	2.3	7600	24.3	630
1000	0	0	0	1.4	7500	26.7	650

Fig. 4 Calculated and measured temperature profiles for the bigger shaft

ligibly small influence on the simulation results. Hence, this model can be applied to other samples such as long profiles.

4 Profile Cooling Simulations

The model is now used to investigate the distortion behavior of the profiles. *T* and *L* profile simulations have been carried out to investigate their cooling distortion behaviors. The geometrical dimensions, finite element (FE) mesh, and the observation points are shown in Fig. 7. The profile is made of C45 steel, which is a typical material for such profiles. The temperature-dependent flow curves can be found in the literature [22], and the temperature-dependent thermophysical material properties are given in Table 4. This steel, unlike high-strength steels, completely loses its elastic characteristics above a temperature of about 600°C. In order to demonstrate the plasticity effects, the cooling conditions have to be much more intensive as compared to the natural cooling conditions. The heat transfer coefficient and the emissivity are taken as 1000 W/m^2/K and 0.7, respectively. Radiation constitutes approximately 10% of the heat transfer. The cooling process starts at 600°C. Therefore, there is no phase transformation effect.

The residual axial stress in the cross section after the cooling is shown in Fig. 8. The outer region is subjected to compressive stresses and the core is subjected to tensile ones. The evolution of the plastic zones can be observed in Fig. 9 during different stages of cooling. At the beginning, the external region shortens faster due to the temperature difference between the core and surface, and the external regions yields under tension. However, it returns later to the elastic range, while the compressive stress in the core region reaches the yield limit. Finally, the exterior region comes under compression, while the compressive stress in the core becomes tensile stress.

In practice, 75–95% of the plastic work is converted into heat. The unconverted part of the dissipated energy is stored in the form of micromechanical stresses in crystal structure. The dissipation of the mechanical energy significantly affects the temperature field only in special cases such as metal forming. The dissipation process and the corresponding heat generation are shown as functions of the cooling time in Fig. 10 for the points described in Fig. 7. It is obvious that the heat generation effect is negligibly small as compared to the convection and radiation in the case of quenching.

The second simulation is the cooling of a standard *L* profile with the dimensions of $L120\times12$ according to DIN 1028. The profile cross section is simply symmetric and prone to distortions. The geometrical dimensions, FE mesh, and observation points are shown in Fig. 11. The behavior of the state variables at the observation points during cooling is demonstrated in Fig. 12. The left column represents plots for the hypoeutectic steel C45, the material properties of which are listed in Table 4, and the right ones for the eutectic steel C80, listed in Table 5. The heat transfer coefficient is $\alpha_0=10$ W/m^2/K, and the value of emissivity is taken as 0.7 for all surfaces. It is obvious that the temperature at the outer

Pearlite & Martensite							
Temperature (°C)	Elasticity Modulus (GPa)	Poisson's Ratio	Yield Strength (MPa)	Hardening Modulus (GPa)	Density (kg/m^3)	Heat Cunductivity (W/m/K)	Heat Capacity (J/kg/K)
0	220	83	650-1000	4.0-60	7860	50	410
200	200	75	625-945	4.7-50	7790	45	550
400	175	67	450-775	4.5-40	7720	38	620
600	133	59	375-505	1.8-0	7650	32	790
800	80	52	150-150	0-0	7570	29	1160
1000	13	44	0-0	0-0	7490	27	1850
Austenite							
Temperature (°C)	Elasticity Modulus (GPa)	Poisson's Ratio	Yield Strength (MPa)	Hardening Modulus (GPa)	Density (kg/m^3)	Heat Cunductivity (W/m/K)	Heat Capacity (J/kg/K)
0	220	80	250	1.4	7740	6	450
200	176	64	200	1.4	7690	10	510
400	132	48	150	1.5	7640	14	570
600	88	32	100	1.5	7590	18	600
800	44	16	50	1.4	7540	22	630
1000	0	0	0	1.3	7490	26	650

Fig. 5 Calculated and measured internal stresses for the bigger shaft

Table 2 Microstructure phase fractions from measurements (*m*) and simulations (*s*)

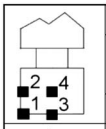	small shaft						big shaft					
	pearlite [%]		bainite [%]		martensite [%]		pearlite [%]		bainite [%]		martensite [%]	
	m	s	m	s	m	s	m	s	m	s	m	s
point 1	-	-	33	31	67	69	94	86	-	5	6	9
point 2	-	-	33	31	67	69	97	86	-	9	3	5
point 3	-	-	22	18	78	82	100	90	-	10	-	-
point 4	-	-	26	22	74	78	100	89	-	11	-	-
	small disk						big disk					
	pearlite [%]		bainite [%]		martensite [%]		pearlite [%]		bainite [%]		martensite [%]	
	m	s	m	s	m	s	m	s	m	s	m	s
point 1	-	-	4	12	96	88	-	-	12	22	88	78
point 2	-	-	5	18	95	82	-	-	16	30	84	70

Table 3 Chemical compositions of shaft steel, disk steel, and steel in the model

	C (%wt.)	Si (%wt.)	Mn (%wt.)	P (%wt.)	S (%wt.)	Cr (%wt.)	Ni (%wt.)	Cu (%wt.)
Shaft	0.97	0.20	0.29	0.01	0.02	1.46	-	0.22
Disc	0.92	0.23	0.35	0.01	0.01	1.48	0.05	0.09
Model	0.95-1.10	0.10-0.35	0.20-0.40	<0.030	<0.025	1.35-1.60	<0.30	<0.30

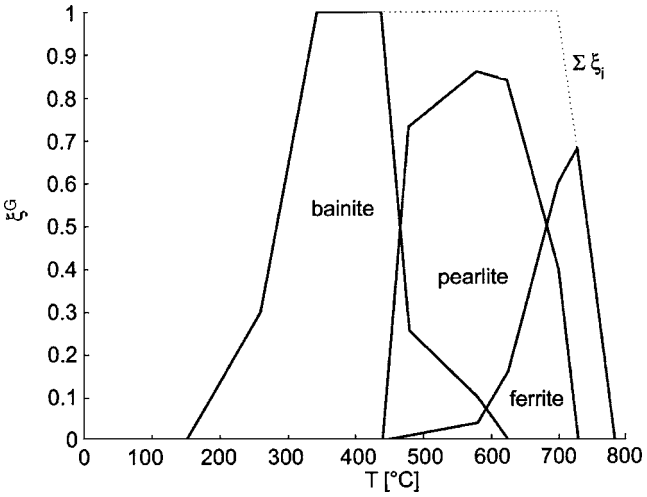

Fig. 6 Measured and calculated distortion profiles for the bigger disk

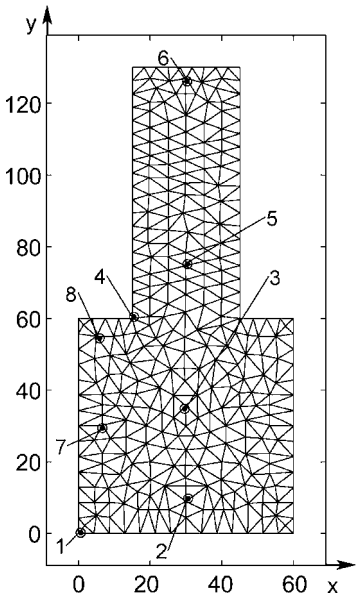

Fig. 7 Finite-element mesh and geometric dimension in (mm) of *T* profile

observation points 1 and 4 drops at the fastest rate, and for the interior point 3 at the slowest rate. Accordingly, the regions lying on the outer parts experience the phase transition earlier than the core. In the third row of diagrams the axial stress is shown. This stress usually changes its direction during the phase transition and achieves a maximum value at the end of the phase transition. The TRIP strains in axial direction are shown in the fourth row. It is noticed that the external regions are subjected to the largest plastic deformations. The distortion of the profiles which is defined in Eq. (32) is shown in the fifth row. The distortion changes direction during cooling, and finally a positive plastic distortion remains. It is also noticed that the deformations are higher for C80 than that of C45.

Figure 13 shows the residual axial stress in the *L* profile. The bold line is the border between the tension region and the compression region. The thermal contraction in the core results in a high tensile stress in this region. The distortion is obviously determined by the cooling of the mass-lumped region. In order to reduce the distortion, the cooling rate around the point 2 should be increased as schematically described in Fig. 14. Such a heat transfer process can be achieved if the point 1 is cooled with an air nozzle from the outside. The distortions for different heat transfer coefficients are shown in Fig. 15. The maximum heat transfer should occur at the vertex in order to reduce the distortion. In some extreme cases, even a distortion in the opposite direction can be obtained [18]. The same effect can be achieved by placing the air nozzle towards point 2 from inside.

5 Conclusions

The experiments and examples demonstrate that:

Table 4 Material properties for C45

Pearlite & Martensite							
Temperature (°C)	Elasticity Modulus (GPa)	Shear Modulus (GPa)	Yield Strength (MPa)	Hardening Modulus (GPa)	Density (kg/m^3)	Heat Conductivity (W/m/K)	Heat Capacity (J/kg/K)
0	215	83	550- 1000	5.1-12.5	7850	48.8	410
200	196	75	420- 940	5.8-10.0	7790	46.5	550
400	177	67	470- 800	4.9- 7.5	7710	41.0	620
600	158	59	470- 0	2.6- 0.0	7630	35.0	790
800	140	52	180- 0	0.0- 0.0	7530	26.0	1160
1000	121	44	0- 0	0.0- 0.0	7430	17.0	1850
Austenite							
Temperature (°C)	Elasticity Modulus (GPa)	Shear Modulus (GPa)	Yield Strength (MPa)	Hardening Modulus (GPa)	Density (kg/m^3)	Heat Conductivity (W/m/K)	Heat Capacity (J/kg/K)
0	200	80	250	4.2	7940	14.8	450
200	160	64	200	4.0	7860	17.3	510
400	120	48	150	3.7	7790	19.6	570
600	80	32	100	3.1	7700	21.9	600
800	40	16	50	2.3	7600	24.3	630
1000	0	0	0	1.4	7500	26.7	650

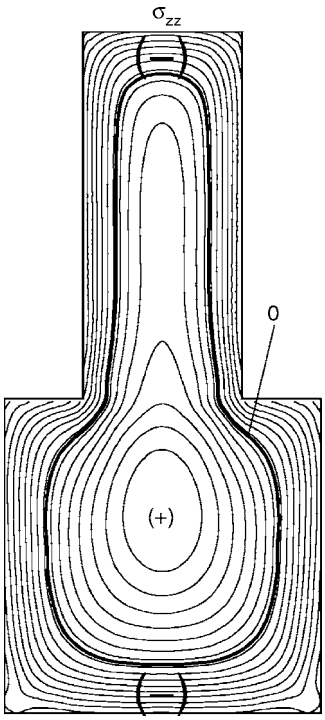

Fig. 8 The residual axial stress in the *T* profile after cooling

- The Avrami equation together with Scheil's additivity rule estimates well the phase evaluations.
- The cooling of steel workpieces can be effectively controlled in a nozzle field.
- The temperature field can be accurately simulated when an appropriate heat transfer coefficient is used.
- The plastic deformation always starts from the surface and penetrates to the core henceforth.
- The heat generation by plastic dissipation is negligible as compared to the latent heat of the phase transition.
- In general the core remains under tensile and the shell remains under compressive residual stresses at the end.

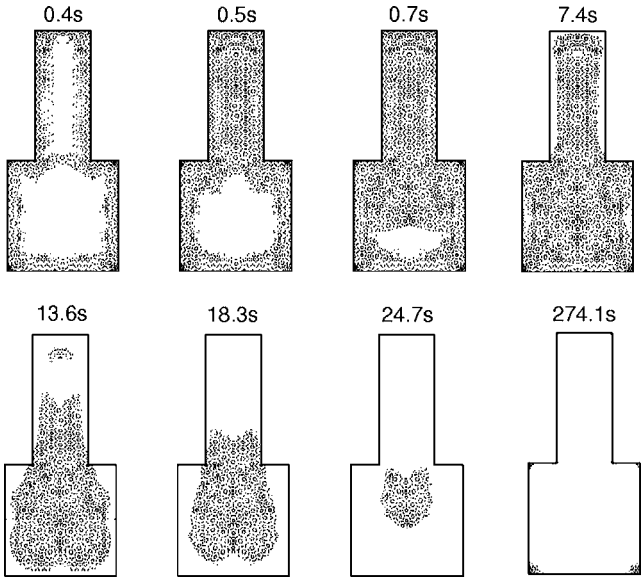

Fig. 9 Evolution of plastic zones during cooling of *T* profile

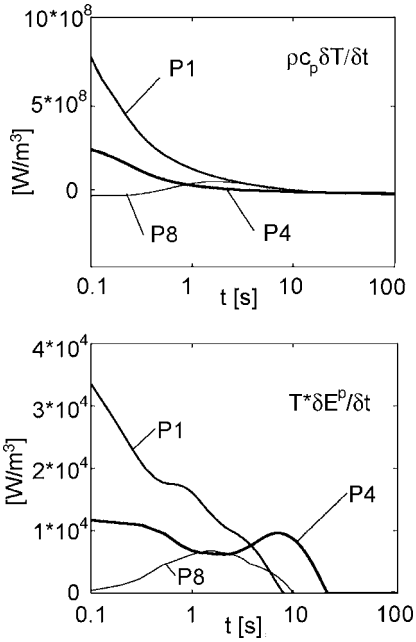

Fig. 10 Dissipation (bottom) and corresponding internal heat generation (top)

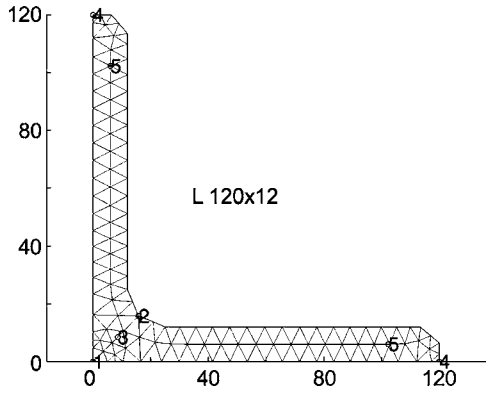

Fig. 11 Finite-element mesh and geometric dimension in (mm) of *L* profile

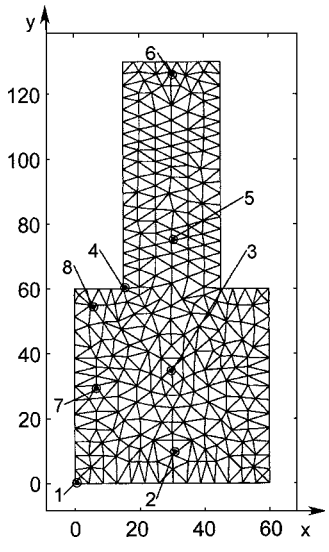

Fig. 12 Behavior of state variables during the cooling of *L* profiles

Table 5 Material properties for C80

Pearlite & Martensite							
Temperature (°C)	Elasticity Modulus (GPa)	Shear Modulus (GPa)	Yield Strength (MPa)	Hardening Modulus (GPa)	Density (kg/m^3)	Heat Conductivity (W/m/K)	Heat Capacity (J/kg/K)
0	220	83	650-1000	4.0- 60	7860	50	410
200	200	75	625- 945	4.7- 50	7790	45	550
400	175	67	450- 775	4.5- 40	7720	38	620
600	133	59	375- 505	1.8- 0	7650	32	790
800	80	52	150- 150	0.0- 0	7570	29	1160
1000	13	44	0- 0	0.0- 0	7490	27	1850
Austenite							
Temperature (°C)	Elasticity Modulus (GPa)	Shear Modulus (GPa)	Yield Strength (MPa)	Hardening Modulus (GPa)	Density (kg/m^3)	Heat Conductivity (W/m/K)	Heat Capacity (J/kg/K)
0	220	80	250	1.4	7740	6	450
200	176	64	200	1.4	7690	10	510
400	132	48	150	1.5	7640	14	570
600	88	32	100	1.5	7590	18	600
800	44	16	50	1.4	7540	22	630
1000	0	0	0	1.3	7490	26	650

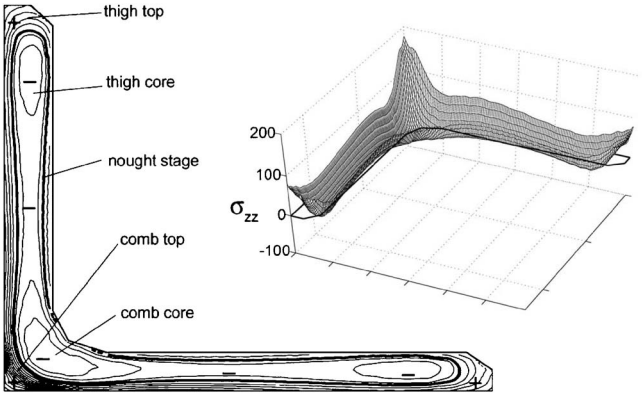

Fig. 13 Residual axial stress in the *L* profile after the cooling

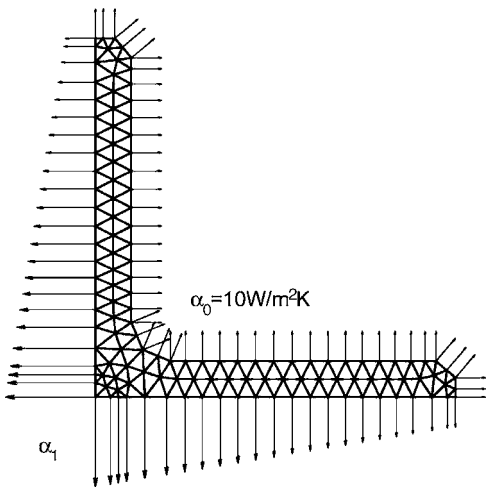

Fig. 14 Schematic representation of cooling strategy

- The distortion changes direction and reaches its maximum value during the phase transition.
- The stresses and strains also reach their maximum value during the phase transition.
- The distortion is mainly due to TRIP strains, which are related to phase transition phenomena.
- The profiles with smaller section sizes have more distortion than those with bigger section sizes, which has been already ascertained in practice.
- The results support the idea that distortion can be reduced by increasing the cooling at mass lumped regions.

Nomenclature

$\mathbf{C}$ = capacitance matrix for heat transfer
$\mathbf{C}, \mathbf{C}^{ep}$ = fourth order elastic and elastoplastic constitutive tensors, respectively
$\mathbf{E}$ = linearized strain tensor
$\mathbf{F}$ = force vector for heat transfer
$\mathbf{H}^e$ = element interpolation functions
$\mathbf{I}, \mathbf{I}$ = fourth and second order identity tensor, respectively
$\mathbf{K}$ = conductivity matrix for heat transfer (Eq. (6)) stiffness matrix for displacement solution

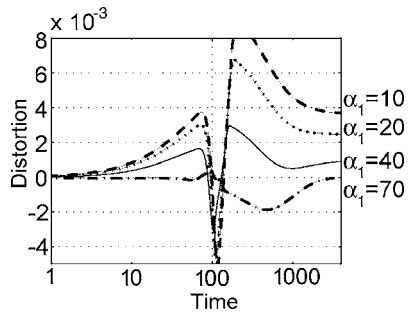

Fig. 15 The distortion of *L* profiles for different cooling conditions (according to Eq. (32))

$\mathbf{N}$ = flow surface unit normal
$\mathbf{n}_S$ = surface unit normal
$\mathbf{q}_S$ = heat flux vector
$\mathbf{u}$ = displacement vector
$\mathbf{T}$ = nodal temperature vector (Eq. (6)) Cauchy stress tensor
a, b = Avrami parameters
A^e = cross section area of an element
c_p = specific heat capacity
d_0, d_1, d_2 T_U, and T_L = Hougardy parameters
e = emissivity
H = hardening parameter
H_i^e = element interpolation function for ith node
h = element thickness in the third dimension
k_M = martensitic transformation constant
k = heat conductivity
L_i = latent heat of ith phase conversion
n = exponent in an expression, Hougardy parameter (Eqs. (9) and (11)) number of phases in mixture (Eqs. (3) and (8))
N = exponent in the expression to define mixture rule (Eq. (7)) number of nodes per element (Eq. (4))
p = distortion defined by curvature
q_v = heat generation rate in the body
r, s = local (natural) coordinates
S^e = convective boundary line for a boundary finite element
t = time
T_i^e = temperature at ith node
T = temperature
T_∞ = ambient temperature
T_{Ms} = martensitic transformation start temperature
x, y, z = global cartesian coordinates
Z_{mix}, Z_i = material property estimate for mixture and its value for ith phase, respectively
α = convection coefficient
α' = equivalent convection coefficient (including radiation)
Δ = profile deflection
$\varepsilon_{\text{eff}}^p$ = equivalent plastic strain
ε = strain
φ = dummy variable in Hougary parameters calculation
ϕ = flow condition
ψ = radiation view factor
κ = bulk modulus
Λ = Greenwood Johnson factor
λ = plastic multiplier
μ = shear modulus
ρ = mass density
σ = Stefan-Boltzmann constant (Eq. (3)) stress
σ_y = yield stress
σ_{eff} = effective stress
ξ_i = phase fraction of ith phase
τ = TTT-curve defining function
χ = fraction of mechanical energy converted to heat energy

References

[1] Fischer, F. D., Oberaigner, E. R., Tanaka, K., and Nishimura, F., 1998, "Transformation Induced Plasticity Revised an Updated Formulation," Int. J. Solids Struct., **38**(18), pp. 2209–2227.
[2] Berns, H., 1977, "Distortion of Steel due to Heat Treatment," Verzug von Stählen infolge Wärmebehandlung, Werkstofftechnik, **8**, pp. 149–157.
[3] Hinteregger, E., 1990, "Internal Stresses and Deformations of Railway Profiles after Rolling Before Bundling," (German: Eigenspannungen und Verformungen in Schienen nach dem Walzen vor dem Richten), Ph.D. thesis, Montanuniversität Leoben, Austria.
[4] Prantil, V. C., Callabresi, M. L., Lathrop, J. F., Ramaswamy, G. S., and Lusk, M. T., 2003, "Simulating Distortion and Residual Stresses in Carburized Thin Strips," ASME J. Eng. Mater. Technol., **125**, pp. 116–124.
[5] Puschmann, E., and Specht, E., 2004, "Atomized Spray Quenching as an Alternative Quenching Method for Defined Adjustment of Heat Transfer," Steel Res., **75**, pp. 283–288.
[6] Puschmann, E., and Specht, E., 2004, "Transient Measurement of Heat Transfer for Metal Quenching with Atomized Sprays," Exp. Therm. Fluid Sci., **28**, pp. 607–615.
[7] Fernandes, F. M. B., Denis, S., and Simon, A., 1985, "Mathematical Model Coupling Phase Transformation and Temperature Evolution During Quenching of Steels," Mater. Sci. Technol., **1**(10), pp. 805–815.
[8] Song, R., Dhatt, G., and Cheikh, A. B., 1990, "Thermo-mechanical Finite Element Model of Casting Systems," Int. J. Numer. Methods Eng., **30**, pp. 579–599.
[9] Gür, C. H., and Tekkaya, A. E., 1996, "Finite Element Simulation of Quench Hardening," Steel Res., **67**, pp. 298–306.
[10] Inoue, T., and Wang, Z., 1985, "Coupling Between Stress, Temperature and Metallic Structures During Processes Involving Phase Transformations," Mater. Sci. Technol., **1**(10), pp. 845–850.
[11] Leblond, J. B., Mottet, G., Devaux, J., and Devaux, J. C., 1985, "Mathematical Model of Anisothermal Phase Transformations in Steels, and Predicted Plastic Behavior," Mater. Sci. Technol., **1**, pp. 815–822.
[12] Kolmogorov, A. E., 1937, Izv. Akad. Nauk SSSR, Ser. Mat., **1**, 355; Johnson, W. A., and Mehl, R. F., 1939, Trans. Am. Inst. Min., Metall. Pet. Eng., **135**, p. 416; Avrami, M., 1939, J. Chem. Phys., **7**, p. 103.
[13] Hougardy, H. P., 1990, *Phase Transition and Microstructure of Unalloyed Steel*, (German: Umwandlung und Gefüge unlegierter Stähle), Steel Research Press, Dusseldorf, Germany.
[14] Scheil, E., 1935, Steel Res., **12**, p. 565.
[15] Koistinen, D. P., and Marburger, R. E., 1959, "A General Equation Prescribing the Extent of the Austenite-martensite Transformation in Pure Iron-Carbon Alloys and Plain Carbon Steels," Acta Metall., **7**, pp. 59–60.
[16] Denis, S., Gautier, E., Sjöström, S., and Simon, A., 1987, "Influence of Stress on the Kinetics of Pearlitic Transformation during Continuous Cooling," Acta Metall., **35**, pp. 1621–1632.
[17] Betten, J., 1993, *Continuum Mechanics: Elasto- Plasto- and Creep Mechanics*, (German: Kontinuumsmechanik: Elasto- Plasto- und Kriechmechanik), Springer Press, New York.
[18] Pietzsch, R., 2000, *Simulation and Minimization of the Distortion of Steel Profiles with the Cooling*, (German: Simulation und Minimierung des Verzuges von Stahlprofilen bei der Abkühlung), Ph.D. thesis, Shaker Press, Aachen.
[19] Greenwood, G. W., and Johnson, R. H., 1965, "The Deformation of Metals Under Small Stress during Phase Transformation," Proc. R. Soc. London, Ser. A, **283**, pp. 403–422.
[20] Brzoza, M., Specht, E., Ohland, J., Luebben, T., Belkessam, O., Fritsching, U., and Mayr, P., 2005, "Adjustment of Nozzle Field During Gas Quenching," (German: Dusenfeldanpassung bei der flexiblen Gasabschreckung), Hartetei-Technische Mitteilungen, München, **60**, no. 3, pp. 166–172.
[21] Exner, H. J., and Hougardy, H. P., 1986, "Introduction to the Quantitative Microstructure Analysis," (German: Einführung In die Quantitative Gefügeanalyse), DGM Informationsgesellschaft Oberursel, pp. 8–18.
[22] Radaj, D., 1992, *Heat Effects of Welding*, Springer Press, New York.